Nanoscale

Formation of hexagonal-molybdenum trioxide (h-MoO3) nanostructures and their pseudocapacitive behavior

Journal:	*Nanoscale*
Manuscript ID:	NR-ART-03-2015-001505.R1
Article Type:	Paper
Date Submitted by the Author:	25-May-2015
Complete List of Authors:	Kumar, Vipin; NTU Singapore, School of Materials Science and Engineering Wang, Xu; NTU Singapore, School of Materials Science and Engineering Lee, Dr. Pooi See; NTU Singapore, School of Materials Science and Engineering

Nanoscale RSCPublishing

Formation of hexagonal-molybdenum trioxide (h-MoO_3) nanostructures and their pseudocapacitive behavior

Vipin Kumar,[a] Xu Wang[a] and Pooi See Lee*[a]

Received (in XXX, XXX) Xth XXXXXXXXX 20XX, Accepted Xth XXXXXXXXX 20XX

The crystallographic structure and morphology of redox active transition metal oxides have a pronounced effect on their electrochemical properties. In this work, h-MoO_3 nanostructures in three distinct morphologies, i.e., pyramidal nanorods, prismatic nanorods and hexagonal nanoplates, were synthesized by a facile solvothermal method. The morphologies of h-MoO_3 nanostructures were tailored by the controlled amount of hexamethylenetetramine. An enhanced specific capacitance about 230 F/g at an applied current density of 0.25 A/g, was achieved in h-MoO_3 pyramidal nanorods. Electrochemical studies confirmed that the h-MoO_3 pyramidal nanorods exhibit superior charge-storage ability. This improved performance can be ascribed to the coexistence of its well exposed crystallographic planes with the abundant active sites, i.e., hexagonal window (HW), trigonal cavity (TC) and four-coordinated square window (SW). The mechanism of charge-storage is likely facilitated by the vehicle mechanism of proton transportation due to the availability of the vehicles, i.e., NH_4^+ and H_2O. The promising, distinct and unexploited features of h-MoO_3 nanostructures unveil a strong candidate for pseudocapacitive electrode materials.

1. Introduction

The physicochemical properties and electronic structure of transition metal oxides have been a subject of intense fundamental research.[1,2] Transition metal oxides are considered the promising candidates for the electrochemical energy-storage (supercapacitors and batteries) applications due to their excellent reduction-oxidation (redox) properties ($M^{n+} + e^- \rightarrow M^{n+-1}$).[3,4] Recently, supercapacitors emerge as a promising electrochemical energy-storage devices due to the spectacular features, such as higher power density compared to the batteries (~10^4 W/kg for supercapacitors and ~100 W/kg for batteries), quick charging/discharging (ms-min) and excellent cycling stability (10^4-10^6) in aqueous as well as non-aqueous electrolytes.[5] Supercapacitors have attracted considerable attention because of their potential use in vehicle start/stop/start operation, micro-electro-mechanical and portable electronic devices.[6,7] To date, binary transition metal oxides (MnO_2, CoO_3, V_2O_5, etc.)[8,9] have gained enormous attention as the prospective electrode materials for supercapacitors applications (based on intercalation pseudocapacitance and surface pseudocapacitance). The capacitive behavior can be improved by tuning the state of crystallinity of the materials, e.g., amorphous or crystalline. However, this approach is found strongly materials system dependent, for example Zheng et al.[10,11] and Farsi et al.[12] showed that the amorphous RuO_2 xH_2O and amorphous MoO_3 nanostructures store more charges than that of their crystalline counter parts, respectively, while recently Brezesinski et al.[13] and Kim et al.[14] found that the crystalline MoO_3 and Nb_2O_5 are superior charge-storage candidates to their amorphous counter parts.

Nanostructuring of the binary transition metal oxides in various crystallographic structures have also been considered an effective and feasible approach to improve the electrochemical performance of the electrode materials.[15] To date, layered binary transition metal oxides have been studied frequently due to their two dimensional crystallographic structure, which provides effective paths for the conduction of electrolyte ions. However, binary transition metal oxides in three dimensional (3D) crystallographic structure (open-structure), which can provide 3D conduction paths for electrolyte ions have not explored The 3D crystallographic structure primarily exists in metastable phase of binary transition metal oxides, such as spinel-MnO_2, beta-V_2O_5, MoO_3, etc. [9,10,13,15]

Among them MoO_3 is considered as an interesting material due to the high electrochemical activity of its stable as well as metastable polymorphs.[16,17,18] Thermodynamic stable phase of MoO_3, i.e., α-MoO_3 possesses a layered (*ABA*) framework structure (i.e., 2D), while its metastable polymorphs possess an open-structure (i.e., 3D) in hexagonal phase (h-MoO_3), a layered (*AAA*) framework structure in MoO_3-II phase and rutile or distorted rutile structure in β-MoO_3 phase.[19] To date, electrochemical properties of α-MoO_3 have been investigated. Various strategies have been employed to enhance the electrochemical performance of α-MoO_3, for example nanowire arrays [20] core/shell architecture [21] decorations of conducting supports

(polymers) [22] incorporation of CNT and nanocomposites with other oxides.[23,24] However, the efforts did not improve the specific capacitance significantly. Recently, a kinetically favoured intercalation mechanism is proposed, benefiting from mesoporous and iso-oriented nanocrystalline domain of layered α-MoO_3,[13] for improved Li^+ ions storage (605 C/g). In addition to all the efforts made till date, several computational and experimental studies have shown that the crystal plane structure of electrode materials has a substantial influence on the electrochemical performance of materials.[25,26,27] Therefore, size and shape controlled of nanomaterials are essential in unleashing and understanding their intrinsic properties, which are critical in electrochemical applications. More recently, highest achievable specific capacitance of 326 F/g (at 0.25 A/g) using α-MoO_3 nanobelts is reported, but the loading mass tends to be low (~ 0.51 mg).[28] Also, the specific capacitance of α-MoO_3 nanoplates as high as 280 F/g (calculated from non-rectangular CV curves) has been achieved, benefiting from the small diffusion length of the ions into the nanosheets.[29] Most recently, Chang et al. introduced the concept of the work function difference to enhance the working potential window of an asymmetric supercapacitor device based on rGO-α-MoO_3, in an aqueous electrolyte solution.[30] Due to inter-layer spacing (6 Å) between the two layers of α-MoO_3, it can accommodate a massive amount of electrolyte ions (0.28 Å for H^+), but its poor conductivity limits the diffusion of the ions. Compared to α-MoO_3 that has intercalation sites along one dimension only, the open-structure of h-MoO_3 offers an increase in the degree of freedom (from 1 to 3) for electrolyte ions to intercalate in all possible directions. The hexagonal phase of MoO_3 (h-MoO_3) can be considered a promising host material for electrolyte ions attributed to the availability of the various intercalation sites, i.e., hexagonal window (HW), trigonal cavity (TC) and four-coordinated square window (SW). The open-structure of h-MoO_3 could facilitate intercalation as well as diffusion of ions to realize improved supercapacitor performance.

Taking into account all these factors, we have synthesized h-MoO_3 nanostructures using a facile solvothermal method. The synthesis of h-MoO_3 nanostructures in the diverse morphologies has been rarely found, this is related to the difficulty in the phase formation due to thermodynamic (formation enthalpy and entropy of constituents) barriers.[31,32,33] We have previously attempted to tune the morphology of h-MoO_3 using thiourea as the source of ammonium ions. With the increase in the loading amount of the ammonium ions, predominant formation of the flower-like morphology was observed. In this work, we are able to circumvent the challenges limiting the pseudocapacitive behaviour by judicious control of the synthesis in tuning the physical structure of h-MoO_3 nanostructures.

2. Experimental

2.1. Chemical used

All chemicals, Mo powder 99.9%, H_2O_2 (30%), HNO_3 (conc.), Potassium hydroxide (KOH) flakes and Hexamethylenetetramine (HMTA) were used as received from Alpha Aesar and Sigma Aldrich, respectively, without further purification.

2.2. Preparation of h-MoO_3 nanostructures

To synthesize h-MoO_3 in pyramidal nanorods, prismatic nanorods and hexagonal nanoplates-like morphology, a simple yet effective solvothermal approach was employed, modified from our previous report[32] with the use of hexamethylenetetramine (HMTA) as structure directing agent instead of thiourea ($CS(NH_2)_2$). In brief, peroxomolybdic solution was prepared by the addition of hydrogen peroxide (H_2O_2) into a 20 ml glass vial containing 0.50 g of Mo powder. In a typical synthesis procedure, 100 mg, 150 mg and 250 mg of HMTA in 10 ml of DI water were used. The solution of HMTA was slowly added into peroxomolybic solution and left for stirring. The reaction times to prepare h-MoO_3 are compared with the other synthesis routes, and presented in Supporting Information; Table S1.The solvothermal reaction was carried out at 100 °C for 18 h. Finally, the precipitates were collected and washed thoroughly with ethanol and DI water to remove loosely bound or bulk particles. The as-obtained precipitates were dried at 70 °C to get the final product.

2.3. Electrode preparation for electrochemical testing

The working electrodes were prepared by mixing the as-prepared h-MoO_3 powder (85 %), carbon black (10 %) and polyvinylidene fluoride (PVDF) (5 %) into a 5 ml glass vial containing 500 µl of N-methyl-2-pyrrolidone (NMP), under magnetic stirring to make slurry. 20 µl of this slurry was coated onto a current collector (graphite paper, 1 cm^2) and dried in a laboratory oven at 100 °C. The loading mass was measured to be 0.95 ± 0.05 mg, for all three samples. Electrochemical testing was carried out in an aqueous solution of H_2SO_4 (1 M) in a potential window of 0.05 V to 0.65 V *vs.* Ag/AgCl.

2.4. Structural characterizations

The samples were characterized using powder X-ray diffractometry (Shimadzu XRD – 6000, Cu Kα radiation λ = 1.54 Å; power 2 kW) at a scan rate of 1°/min. in the 2θ range of 10° - 60°. Field emission scanning electron microscopy (FESEM; JEOL, JSM 7600F thermal FEG, JSM 6340F cold cathode FEG) and Transmission electron microscopy (TEM; JEOL, JEM 2010 and JEM 2100F) was used to evaluate the morphology of the samples. Thermal analysis was done using thermo gravimetric analysis (TGA) (Q 500, Max. Temperature 900 °C) and IR spectroscopy (Perkin Elmer, Model Spectrum GX) was used to get the information about the state of the bonds present. X-ray photoelectron measurements (XPS) were carried out using VG ESCALAB 220I-XL spectrometer with a twin monochromated Al Kα X-ray source (1486.6 eV) at a constant dwell time of 50 ms and a pass-energy of 50 eV. CasaXPS peak fitting software was used to perform curve fitting. The physical surface area (Brunauer-Emmett-Teller) and pore size distribution was measured using Tristar-II surface area and porosity analyser. Electrochemical measurements were carried out using Solartron, S1470E electrochemical interface and AutoLab PGSTAT 30 potentiostate. Three electrode cell was used for electrochemical testing, in which graphite paper coated with active materials, platinum sheet and saturated Ag/AgCl were employed as working, counter and reference electrode, respectively,

in an aqueous electrolyte (1 M H_2SO_4). Electrochemical impedance spectroscopy (EIS) measurements were carried out by applying an AC voltage with 1 mV amplitude in a frequency range from 100 mHz to 100 kHz at open circuit potential (OCP).

3. Results and discussion

3.1. Structural characterizations

The crystallographic phases of the as-prepared samples were evaluated using X-ray diffraction (XRD), as shown in Figure 1. All the XRD peaks in the patterns were matched exclusively with the hexagonal phase of MoO_3 (ICDD # 15-5332) with the lattice parameters a = 10.54 Å, c = 3.72 Å and the cell volume V = 359.37 Å^3.[34] A few impurity peaks (♦) were observed in the pattern of hexagonal nanoplates (probably due to residue of the by-product formed by Mo^{5+} ions, which make complex ammonium hydroxides of Mo, i.e., $(NH_4)_8Mo_{10}O_{34}$). The major peaks positioned at 2θ ~ 25.5° and 19.2° are the characteristics of hexagonal phase of MoO_3.

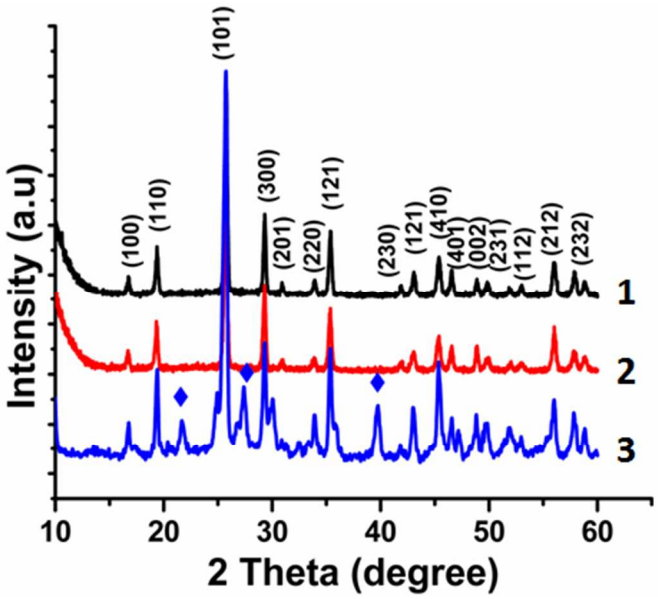

Figure 1. Show X-Ray diffraction patterns of pyramidal nanorods (1), prismatic nanorods (2) and hexagonal nanoplates (3). The nanoplates show some impurity peaks labelled in blue diamond (♦).

The morphology of the as-prepared h-MoO_3 nanostructures was evaluated using FESEM, as shown in Figure 2. Figure 2 (a), (b) and (c) depict pyramidal nanorods, prismatic nanorods and hexagonal nanoplates-like morphology of the samples prepared using 100 mg, 150 mg and 250 mg of HMTA, respectively. The typical diameter of pyramidal nanorods was about 400 and 100 nm at the base and tip, respectively, while the diameter of prismatic nanorods was about 350 nm. The length and thickness of the hexagonal nanoplates were about 1 µm and 80 nm, respectively. The effect of the concentration of ammonium ions on the nucleation and growth is critical in controlling the morphology of the as prepared nanostructures, as explained in our previous report using thiourea as the source of ammonium ions.[32]

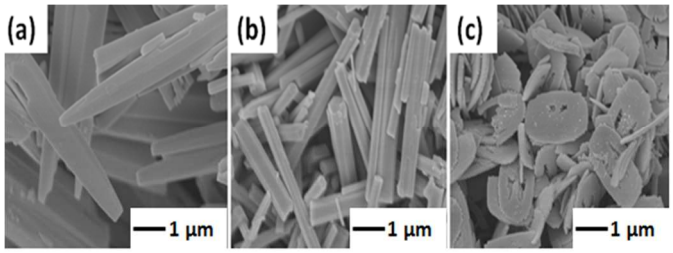

Figure 2. FESEM micrographs of the samples prepared using (a) 100 mg (b) 150 mg and (c) 250 mg of HMTA in peroxomolybdic acid solution.

The concentration of HMTA or ammonium (NH_4^+) ions is essential to control the morphology of the final products. HMTA is a non-ionic, hetero-cyclic organic compound with the chemical formula $(CH_2)_6N_4$, which eventually dissociates into NH_4^+ and OH^- ions upon hydrolysis at the ambient conditions.[35] The reaction of molybdenum (Mo) powder with the hydrogen peroxide (H_2O_2) generates variety of species attached with 1 to 6 peroxide groups.[36,37] The attachment of the peroxide groups with the molybdic units strongly depends on the pH of the medium. A yellow peroxomolybdic solution was obtained in the acidic medium (pH ~ 1-1.5), which mainly consists of monomers and dimers peroxo species, i.e., $[MoO(O_2)_2(H_2O)_2]$, $[O\{MoO(O_2)_2(H_2O)_2\}]^{2-}$ and other even more complex poly-peroxo species.[38]

The chemistry of HMTA with the peroxomolybdic acid solution is accountable to generate the nuclei and to form the lattice of molybdenum trioxide (MoO_3) in hexagonal phase. The interaction of NH_4^+ and OH^- ions (hydrolysed product of HMTA) with the peroxomolybdic species can be expressed according to the following reaction (1).

$$[Mo_2(O)_3(O_2)_4(H_2O)_2]^{2-} + 3NH_4^+ + OH^- \rightarrow 2[MoO_{3-x}(NH_4)_x(H_2O)_y] \quad (1)$$

Where x and y are accountable in altering the morphology of h-MoO_3 nanostructure. The NH_4^+ ions reside in the tunnel of the hexagonal framework and are responsible to maintain the stability of the framework.[39]

When a small amount (100 mg) of HMTA was incorporated into the peroxomolybdic acid solution, a pyramidal or pencil-like morphology of h-MoO_3 predominates. This morphology attributes to the depletion of the NH_4^+ ions during the synthesis reaction. The NH_4^+ ions continuously alter the interaction of the growth species $[Mo_8O_{26}]^{4-}$ on the crystal surfaces. At the instant NH_4^+ ions are depleted, the growth of the low-energy planes at the tip of the pyramidal nanorods leads to the crystal structure stability. As the loading amount of HMTA was increased (150 mg), a perfect prismatic or hexagonal morphology can be realized. It is interesting to note that the hexagonal nanoplates were obtained with relatively higher amount (250 mg) of HMTA. The as-obtained NH_4^+ ions are pivotal in the formation of hexagonal framework and simultaneously partially-reduce molybdenum cations (Mo^{6+} to Mo^{6-x}). The further growth of hexagonal framework is hindered by dissolution of the

compound formed by Mo^{6-x} cations in the vicinity (due to excessive ammonium ions), as the course of reaction proceeds. The surfaces of the as-prepared hexagonal nanoplates were found to be extremely rough or defective that could probably due to the dissolution of the product formed by Mo^{6-x} ions. This phenomenon was not prevalent during the formation of pyramidal and prismatic nanorods due to a relatively low amount of NH_4^+ ions in the reaction.

The morphologies of the as obtained nanostructures were further characterized by TEM. Figure 3 (a), (b) and (c), unambiguously depict the pyramidal nanorods, prismatic nanorods and hexagonal nanoplates-like morphology, respectively, which are consistent with the FESEM analysis.

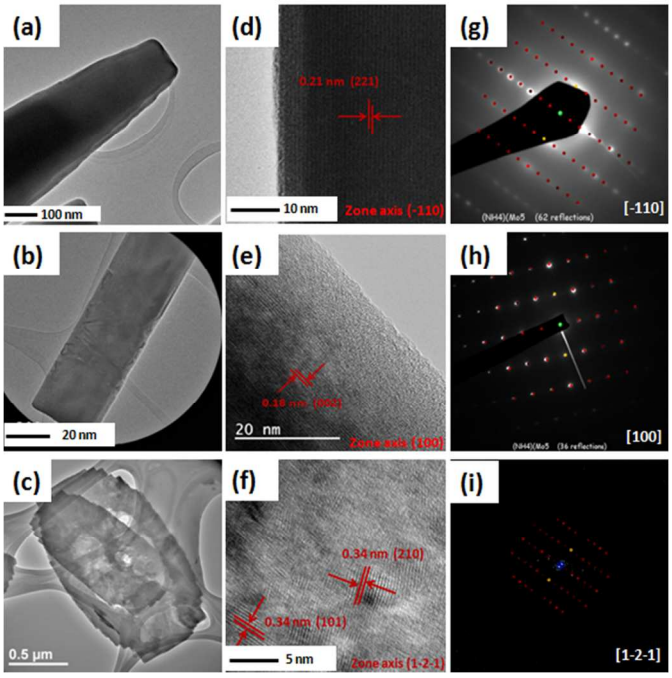

Figure 3. TEM micrographs (a), (b) and (c), HRTEM micrographs (d), (e) and (f) and SAED and FFT patterns (g), (h) and (i) of the samples prepared using 100 mg, 150 mg and 250 mg of HMTA, respectively, are shown. The red and yellow spots in SAED images show standard patterns of h-MoO_3.

Figure 3 (d), (e) and (f) show the HRTEM micrographs of pyramidal nanorods, prismatic nanorods and hexagonal nanoplates, respectively. The spacing between two neighbours fringes were found to be 0.21 nm and 0.18 nm, as can be seen in Figure 3 (d) and (e), corresponding to the d-spacing of the (221) plane and (002) plane of h-MoO_3, respectively. The growth direction of the bulk of pyramidal nanorods was found similar to the prismatic nanorods (Electronic Supporting Information, Figure S1). The interplanar spacing in hexagonal nanoplates were related to the (101) and (210) plane of h-MoO_3, as shown in Figure 3 (f). Furthermore, the selected area electron diffraction (SAED) and fast fourier transformation (FFT) patterns (Figure 3 (g), (h) and (i)) show the diffraction spots along the [$\bar{1}$10], [100] and [1-2-1] zone axis for the tip of pyramidal nanorods, prismatic nanorods and hexagonal nanoplates, respectively.

The chemical purity and thermal stability of pyramidal nanorods, prismatic nanorods and hexagonal nanoplates was evaluated using TGA. Figure 4 shows the typical characteristic of the ammonium ions assisted formation of h-MoO_3.[32] The amount of water and ammonia molecules was calculated to be 3.4%, 1.3% for pyramidal nanorods, 4.5%, 2.5% for prismatic nanorods and 3.35%, 4.95% for hexagonal nanoplates, respectively, taking their weight loss characteristics into account. The weight losses in the temperature range of 150 °C-300 °C and 300 °C-450 °C for all three samples are corresponding to the removal of water and ammonium molecules, respectively.

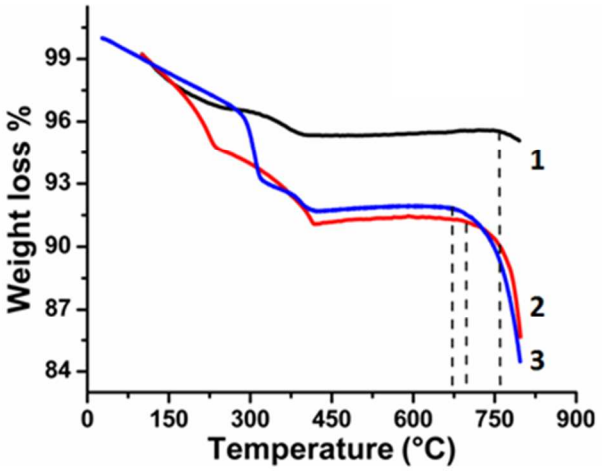

Figure 4. TGA analysis of (1) pyramidal nanorods, (2) prismatic nanorods and (3) hexagonal nanoplates. The step-wise weight loss of the materials is corresponding to removal of water and ammonium molecules from the lattice of h-MoO_3.

The major weight losses of the material occur at 760 °C, 698 °C and 670 °C for pyramidal nanorods, prismatic nanorods and hexagonal nanoplates, respectively. The weight loss at different temperatures suggests that the stability of the MoO_6 octahedra decreases from pyramidal nanorods to prismatic nanorods to hexagonal nanoplates. Approximate formula units $(NH_4)_{0.11}(H_2O)_{0.28}$ $MoO_{2.89}$, $(NH_4)_{0.23}(H_2O)_{0.39}$ $MoO_{2.77}$ and $(NH_4)_{0.44}(H_2O)_{0.30}$ $MoO_{2.56}$ are derived for pyramidal nanorods, prismatic nanorods and hexagonal nanoplates, respectively, taking thermal analysis into consideration. Effects of the concentration of NH_4^+ ions on the bonding between Mo and O was further evaluated using IR spectroscopy, as shown in the Supporting Information, Figure S2 and Table S2.

XPS measurements were performed to analyse the valance state and chemical shift of Mo and N atoms in all three types of samples. Figure 5 (a), (b) and (c), show the XPS spectra of Mo atoms in pyramidal nanorods, prismatic nanorods and hexagonal nanoplates, respectively. Figure (a), (b) and (c) consist of two peaks which correspond to spin orbit doublets of Mo^{6+} ($3d_{5/2}$) and Mo^{6+} ($3d_{3/2}$).[40] The Mo^{6+} ($3d_{5/2}$) and Mo^{6+} ($3d_{3/2}$) peaks are centred at 235.4 eV and 238.5 eV for pyramidal nanorods, 234.9 eV and 238.2 eV for

prismatic nanorods, and 234.2 eV and 238 eV for hexagonal nanoplates. With respect to the binding energies of the deconvoluted Mo^{6+} peaks in pyramidal nanorods, a negative shift of about 0.5 eV and 0.7 eV in the binding energies is identified for prismatic nanorods and hexagonal nanoplates, respectively. This shift in the binding energies indicates that the valance state of Mo decreases from pyramidal nanorods to prismatic nanorods to hexagonal nanoplates. Besides a shift in binding energies, integrated intensity of deconvoluted Mo^{6+} peaks decreases from pyramidal nanorods to hexagonal nanoplates, which suggests that the pyramidal nanorods possess higher contents of Mo^{6+}. The change in the binding energies can be ascribed to the change in NH_4^+ contents in all three samples. To verify this change in NH_4^+ contents, XPS analyses of N 1s atoms were performed, as depicted in Figure 5 (d-f). The N 1s peak for all three samples centred at 401 eV originates from NH_4^+ ions.[41] The integrated intensity of N 1s increases from pyramidal nanorods to prismatic nanorods to hexagonal nanoplates, which indicates that the hexagonal nanoplates possess a higher loading amount of NH_4^+ ions. Attributed to relatively higher loading amount of NH_4^+ ions in hexagonal nanoplates, the binding energies of deconvoluted Mo^{6+} peaks are found less positive than that of pyramidal nanorods. A shake-up satellite peak for all three samples is identified at about 404 eV that could be due to nonstoichiometric NH_4^+ ions generated by N-O complexes, but not much is known about them.[42] The relative amount of these oxidized nitrogen complexes is found much smaller than that of the N-H complexes. XPS analyses show the same trend in the amount of NH_4^+ ions as revealed by TGA and IR analyses.

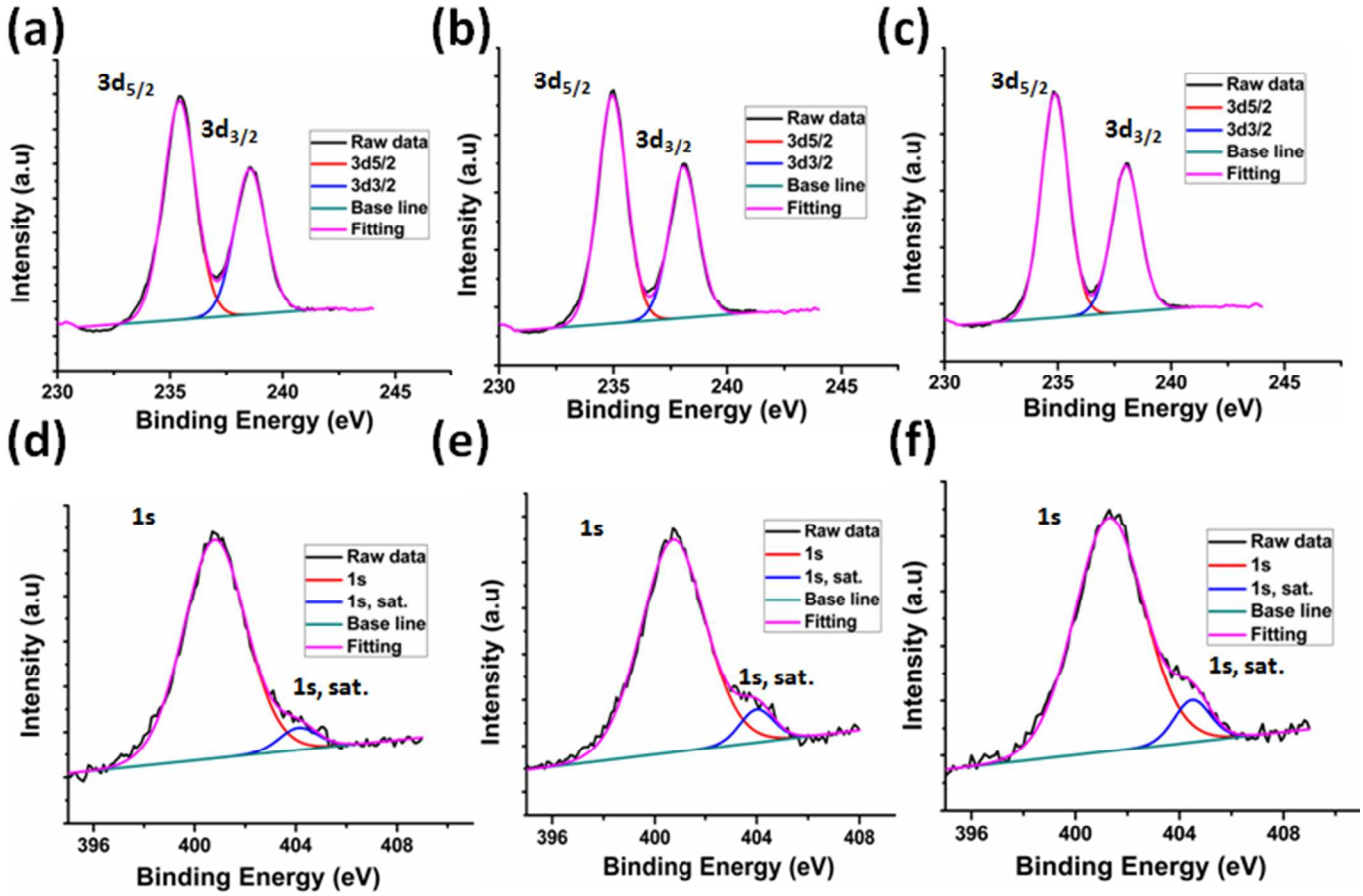

Figure 5. XPS analysis of Mo components in (a) pyramidal nanorods, (b) prismatic nanorods and (c) hexagonal nanoplates, and analysis of N components in (c) pyramidal nanorods, (d) prismatic nanorods and (e) hexagonal nanoplates.

3.2. Electrochemical testing of the samples

It is widely accepted that the electrochemical properties of the materials can be altered by tuning the morphology and size of the materials.[43,44,45] The electrochemical measurements of h-MoO_3 in three different morphologies, i.e., pyramidal nanorods, prismatic nanorods and hexagonal nanoplates, for supercapacitors application, were carried out in a three electrode cell configuration using 1 M H_2SO_4 solution. Cyclic voltammograms (CVs) of pyramidal nanorods, prismatic nanorods and hexagonal nanoplates were carried out at scan rates of 1-50 mV/s, as shown in Figure 6 (a) and (b), respectively. The strong redox peaks in CVs of h-MoO_3 in different

morphologies indicate that the charges are stored in association to the faradic redox reactions.[46,47] A slight shift in the peak potentials signifies the effect of morphologies on the electrochemical activities of the electrode materials.[43,48] The origin of this polarization lies in the fact that the reaction potential (over potential) is extremely sensitive towards the activity of the surfaces. From the electrochemical measurements, we found that the pyramidal nanorods exhibit superior charge-storage capacity compared to prismatic nanorods or hexagonal nanoplates. In the case of hexagonal nanoplates, there is one set of strong redox peaks at 0.22 V/0.39 V (ΔE=170 mV) and another set of faint peaks appeared at 0.45/0.49 (ΔE=40 mV). For the pyramidal nanorods there are two sets of strong redox peaks positioned at 0.24 V/0.29 V (ΔE=50 mV) and 0.46 V/0.50 V (ΔE=40 mV), respectively. These peaks correspond to the reversible ingress/digress of H^+ ions into/out to the framework of h-MoO_3, according to reaction (2).

$$MoO_3\ (NH_4)_x\ (H_2O)_y + zH^+ + ze^- \rightarrow H_z\ Mo_z^{V}\ Mo_{1-z}^{VI}\ O_3\ (NH_4)_x\ (H_2O)_y \quad (2)$$

The intercalation of H^+ ions into the h-MoO_3 is favoured by the redox centres (Mo^{6+} ions), which are located at the various intercalation sites, i.e., hexagonal window (HW), hexagonal cavity (TC) and square window (SW), in the framework of h-MoO_3. These intercalation sites are available in the range of potentials, i.e., $0.1 \leq V \leq 0.3$ (SW), $0.3 \leq V \leq 0.6$ (TC) and $V \geq 0.7$ (HW).

It is commonly believed that the proton conduction in hydrated compounds occur via the Grotthuss (H_2O, $H_5O_2^+$, H_3O^+, OH^- etc.) or Vehicle (H_2O, NH_4^+, $N_2H_5^+$, $CH_3NH_3^+$, etc.) type mechanism facilitated by the water molecules or proton carriers. [10,49] In our case, due to the availability of proton carriers (vehicle), i.e., NH_4^+ and H_2O molecules, the charge-storage mechanism may favour the vehicle mechanism of the proton transportation. Vehicle mechanism is readily encountered in aqueous solutions, liquid/melts and solids. In solids, vehicle mechanism is usually limited to the materials with layered or open-structures.[50] It is believed that the compounds with smaller amount of water molecules (<2 H_2O) conduct protons by the vehicle mechanism.[51] Here, we considered that the charge-storage mechanism in h-MoO_3 does not rely on the Grotthuss mechanism of proton transportation due to the open-structure of h-MoO_3, a small amount of water molecules and the availability of proton carriers (NH_4^+ and H_2O). Additionally, in the crystal structure of h-MoO_3 (shown in the Supporting Information, Figure S3), water molecules are coordinatively attached with the octahedral units, which does not favour the formation of Zundel ($H_5O_2^+$) cations (essential for the Grotthuss mechanism).[52] Therefore, the charge-storage mechanism in h-MoO_3 is more likely facilitated by the vehicle mechanism of proton transportation.

The scan rate response of the as-prepared electrodes was also carried out at different scan rates (1 mV/s to 100 mV/s), as depicted in Figure 6 (c). The anodic and cathodic peak currents (in a potential window of 0.4 V to 0.6 V) increase linearly with the increase in scan rates (CVs are shown in the Electronic Supporting Information, Figure S4). Additionally, linear dependence of the peak currents ($I_{cathodic}$ and I_{anodic}) on the square root of the scan rate ($v^{1/2}$) describes the process is a diffusion controlled electron transfer process.[46,47] The slope of curves, shown in Figure 6 (c), can be used to estimate the diffusion coefficient (D) of the redox-species (H^+ ions) using Randel Sevcik equation (3),[46] and this relationship can also be used to evaluate the electrochemical surface area of the electrode.[54]

$$I_p = 2.69 \times 10^5\ n^{3/2}\ A\ C\ D^{1/2}\ v^{1/2} \quad (3)$$

Where, I_p is the peak current, n is the number of the electrons involved in the reaction (n = 1), A is the area of the electrode (cm^2), C is the concentration of the redox-species (1M), D is the diffusion coefficient of H^+ ions in MoO_3 (1.55×10^{-10} cm^2/s),[53] and ν is the scan rate. If peak currents will be plotted as a function of scan rates, then the electrochemically active surface area of the electrodes will be directly proportional to the slope of the cathodic or anodic peak currents vs. scan rate curves, as shown in Figure 6 (c). Thus, the electrochemically active surface area of the pyramidal nanorods is found about 1.5 times the area of prismatic nanorods and about 2 times the area of hexagonal nanoplates. It is noteworthy that the BET surface area (Supporting information, Figure S5) of pyramidal nanorods (2.2 m^2/g) and prismatic nanorods (1.92 m^2/g) commensurates with the electrochemically active surface area (with the similar pore size of 15 nm and 20 nm for pyramidal nanorods and prismatic nanorods samples, respectively). However, the hexagonal nanoplates sample with a higher BET surface area (7.86 m^2/g) and larger pore size (~40 nm) does not translate to electrochemically active surface area, likely due to the ineffective bonding of electrolyte ions at the pore walls with reduced electric field that leads to sluggish redox reactions.[55] Therefore, it is evident from the peak current vs. scan rate analysis that the pyramidal nanorods exhibit more electrochemical active area which results in improved electrochemical performance.

Figure 7 (a) shows the galvanic charge/discharge curves of pyramidal nanorods, prismatic nanorods and hexagonal nanoplates at an applied current density of 0.25 A/g (charge/discharge curves at higher current densities are shown in the Electronic Supporting Information, Figure S6). The non-linearity associated with the charge/discharge curves further confirms pseudocapacitive response of the as-prepared h-MoO_3 nanostructures. Specific capacitance (C_{sp}) of the as-prepared electrodes can be calculated from charge/discharge curves using equation (4).

$$C_{sp} = 2I \int V.dt/A\ \Delta V^2 \quad (4)$$

Where I, A, and ΔV are the current density at which charges/discharges are obtained, area of the electrode and voltage interval of the discharge, respectively. The change in slope of the discharge curves is attributable to the redox reaction, as can be seen in CVs as well (Figure 6 (a) and (b)).[56] The specific capacitance of pyramidal nanorods, prismatic nanorods and hexagonal nanoplates is calculated to be 230 F/g, 160 F/g and 103 F/g, respectively, at an applied current density of 0.25 A/g. Attributed to relatively higher loading amount of Mo^{6+} ions as well as higher electrochemically active surface area, an improvement in the specific capacitance of pyramidal nanorods is realized. The attainable charge-storage capacity of pyramidal nanorods is distinctly better than that of α-

MoO_3 nanorods, nanowires and nanoribbons.[57,58] A comparison of the electrochemical performance of our electrode material with the α-MoO_3 is shown in the Electronic Supporting Information, Table S3.

We attribute the exposure of desirable crystallographic planes to be of the paramount importance. The hexagonal framework of MoO_3 resembles the hexagonal framework of WO_3.[59] The amount of the stabilizing ions; i.e., ammonium ions; occupancies in the hexagonal framework affect the available intercalation sites and therefore the electrochemical performance. The h-MoO_3 framework is constructed by MoO_6 octahedra sharing the equatorial oxygen in the *ab* plane and stacks along the *c* axis by sharing MoO_6 octahedra. The hexagonal framework contains three different intercalation sites, i.e., hexagonal window (HW), trigonal cavity (TC) and four-coordinated

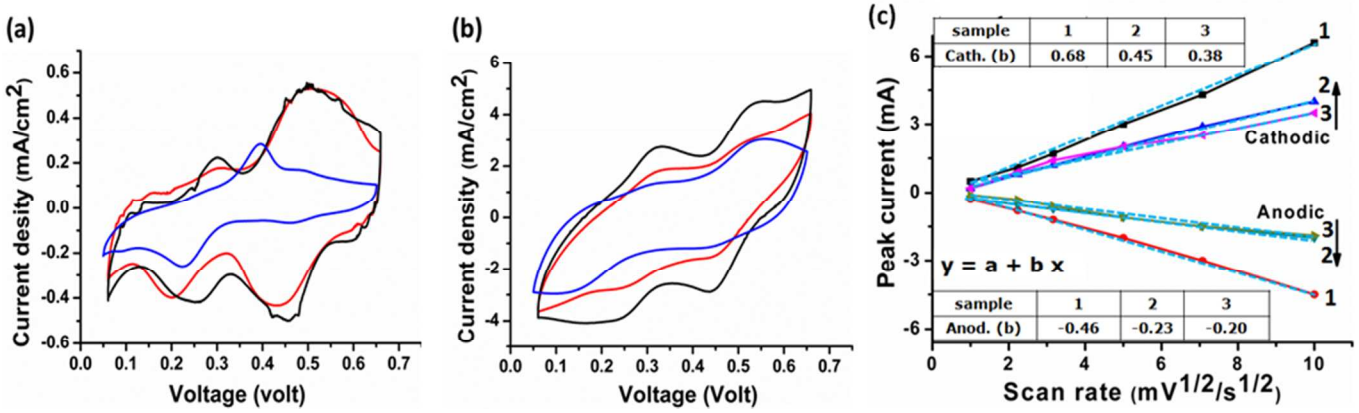

Figure 6. Cyclic voltammograms (CV) of (1) pyramidal nanorods, (2) prismatic nanorods and (3) hexagonal nanoplates are carried out at scan rate of (a) 1 mV/s and (b) 50 mV/s. The redox peaks in CV analysis indicate reversible ingress and degrees of electrolyte ions, and (c) peak current response of the as-prepared electrodes with respect to the square root of the scan rates indicates diffusion controlled charge transfer process. The dotted lines in figure (c) indicate fitting profiles according to equation y = a + bx.

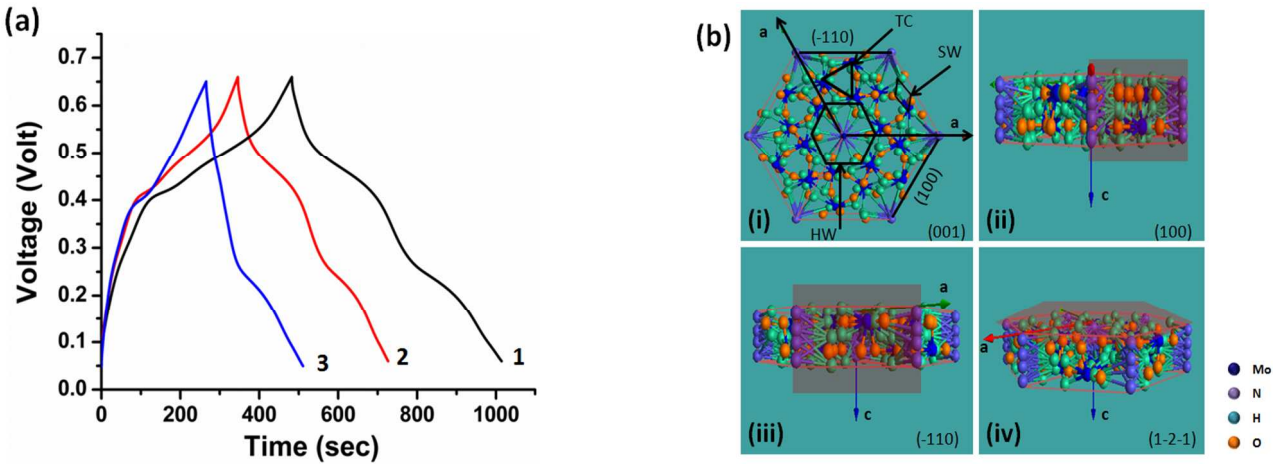

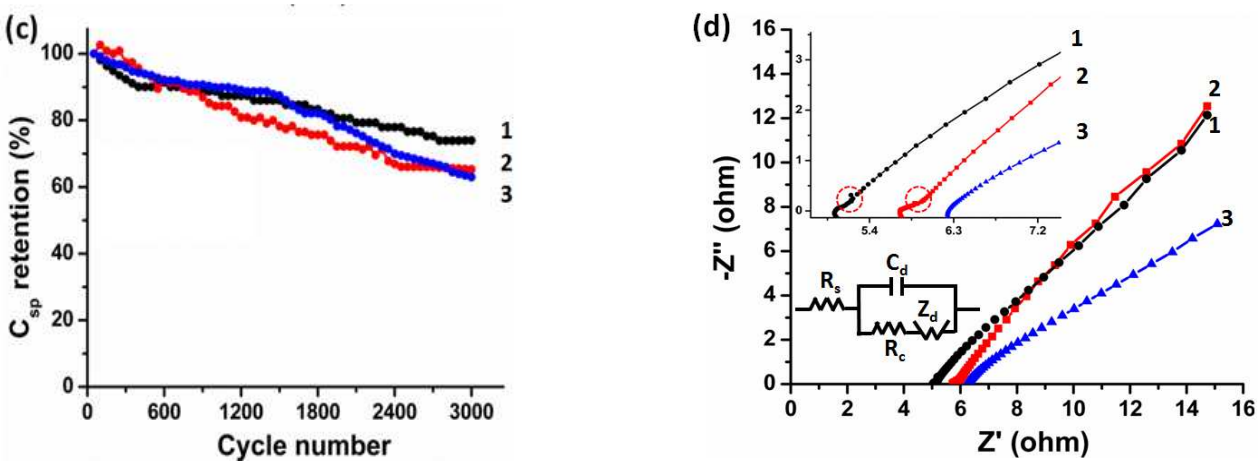

Figure 7. Charge/discharge profiles of (1) pyramidal nanorods, (2) prismatic nanorods and (3) hexagonal nanoplates are performed at an applied current density of (a) 0.25 A/g, (b) Atomic representation of hexagonal framework in the various plane configurations, (c) Cycling test of pyramidal nanorods, prismatic nanorods and hexagonal nanoplates using cyclic voltammetry (CV) at a scan rate of 50 mV/s and (d) Nyquist plots of pyramidal nanorods (1) , prismatic nanorods (2) and hexagonal nanoplates (3) in a frequency bandwidth of 100 mHz to 100 kHz at open circuit potential (OCP). The inset shows the response of the as-prepared electrodes (pyramidal and prismatic nanorods) in the high frequency region (100 kHz-10 mHz). In the inset of figure (d) (Randles circuit), R_s, Z_d, R_c and C_{dl} indicates solution resistance, diffusion resistance or Warburg resistance, charge transfer resistance and double layer capacitance, respectively.

square window (SW) running along the *c* axis, and these intercalation sites are available for the guest ions,[60] as shown in Figure 7 (b)-(i). Among the various available intercalation sites, most of the HW sites were preoccupied by the NH_4^+ ions to stabilize the hexagonal framework, and exposes along the [001] direction of h-MoO_3. On the other hand, TC and SW are positioned along the [001] and [100] directions, respectively. It is believed that the TC sites can accommodate large amount of electrolyte ions.[51] In our case, pyramidal nanorods are constructed by the (100) and $(\bar{1}10)$ planes (shadow plane in the atomic representation, Figure 7 (b)-(ii) and (iii)), representing their base and tip plane, respectively, while prismatic nanorods possess only (100) plane (shadow plane in the representation, Figure 7 (b)-(ii)). The coexistence of the $(\bar{1}10)$ plane besides (100) plane in case of pyramidal nanorods offer an additional degree of freedom to electrolyte ions to intercalation into TC and SW sites.[53] The existence of two distinct redox peaks in CV analysis signifies the intercalation into the SW ($0.1 \leq V \leq 0.3$) and TC ($0.3 \leq V \leq 0.6$) sites, similar behavior was also identified in structurally identical Na doped V_2O_5.[9] The improved current with distinct redox peaks in case of pyramidal nanorods can be considered as a consequence of this process, as can be seen in Figure 6 (a). The persistence of redox peaks even at higher scan rate (50 mV/s), Figure 6 (b), indicates the ease of intercalation into pyramidal nanorods due to the reasons discussed above. A pitiable capacitive charge-storage performance of hexagonal nanoplates is originated from not only higher content of ammonium ions within the framework but also the plane exposed by hexagonal nanoplates. The $(1\bar{2}\bar{1})$ plane of hexagonal nanoplates predominantly exposes HW and TC sites, which are preoccupied by NH_4^+ ions, the shadow plane in Figure 7 (b)-(iv) shows $(1\bar{2}\bar{1})$ plane of h-MoO_3. The availability of SW sites in hexagonal nanoplates gives rise to the strong redox peaks (0.22 V/0.39 V) and attributed to the lack of appropriate TC sites, a set of faint or depressed redox peaks appeared at 0.45 V/0.49 V, as can be seen in Figure 6 (a).

The cycling stability of h-MoO_3 in the various morphologies (pyramidal nanorods, prismatic nanorods and hexagonal nanoplates) is evaluated by the cyclic voltammetry (CV) test, at a scan rate of 50mV/s in 1 M H_2SO_4 electrolyte solution, as shown in Figure 7 (c). A capacitance of 74%, 65% and 62% of the initial value is retained for pyramidal nanorods, prismatic nanorods and hexagonal nanoplates after 3000 cycles of continuous charge/discharge. This is attributable to increase in the contact resistance that comes from poor contacts (between the current collector and active materials) upon expansion/contraction of the active material (due to ingress/digress of electrolyte ions).[54,56] Despite achieving good cycling stability, an early stage (~ 300 cycles) degradation (12%) of capacitance is observed in pyramidal nanorods. To address the early stage degradation in the capacitance of pyramidal nanorods, h-MoO_3 electrode without addition of carbon black and PVDF was subjected to 300 cycles. It is evident from the FESEM micrographs (Electronic Supporting Information, Figure S7 (a) and (b)) that the initial stage degradation is caused by breakage of pyramidal nanorods. The framework of metal oxide may collapse during ingress/digress of electrolyte ions.[57] Attributed to a relatively high intake of electrolyte ions in pyramidal nanorods, a small number of Mo^{5+} ions comes out from the framework (caused by mobile Mo^{5+} ions). The excess negative charge of the system (produced by removal of Mo^{5+} ions) is compensated by electrolyte ions (H^+) and results in the framework under stress. Eventually, the framework of the nanorods breaks at the low energy site (neck of the nanorods) and isolates the tip and base of pyramidal nanorods. Due to formation of the abundant active sites at the tip as well as at the base of the nanorods (broken pyramidal

nanorods), a long term cycling stability of the sample was realized, as shown in Figure 7 (c).

The benefit of h-MoO_3 in pyramidal shape becomes more apparent when Electrochemical Impedance Spectroscopy (EIS) is used to evaluate charge transfer and electrode kinetics of h-MoO_3. Nyquist plot in Figure 7 (d) shows the charge transfer characteristics of pyramidal nanorods, prismatic nanorods and hexagonal nanoplates in higher and lower frequency regions. The semicircle in the high frequency region (as shown in the inset of Figure 7 (d)) signifies the charge transfer resistance associated with the faradic reactions. To determine the parameters (R_s, C_{dl}, R_c and Z_d) of EIS, Randles circuit diagram was used, as presented in inset of Figure 7 (d). The values of the parameters are listed in Table 1. Pyramidal nanorods gives the low intercept value (5.03 Ω) on the real axis (*X*-axis), which indicates its low internal resistance (solution resistance and uncompensated resistance) in comparison to prismatic nanorods (5.79 Ω) and hexagonal nanoplates (6.31 Ω). The slight kinks (dotted circle in the inset of Figure 7 (d)) in the high frequency region of the Nyquist plot (for pyramidal and prismatic nanorods) are likely due to the adsorption of electrolyte ions with the surface of the nanorods. Attributed to the adsorption of electrolyte ions with the surface of the nanorods, generation of new resistive element in series with the charge transfer resistance takes place. In the low frequency region, the sloping lines are related to diffusive resistance (Warburg resistance) abided by electrolyte ions entering the interior of the host material. However, in the very low frequency region (f<10 Hz) the resistance of h-MoO_3 in pyramidal morphology increased slightly (due to sluggish redox reactions), as evaluated by Bode plot (shown in the Electronic Supporting Information, Figure S8).

Table 1. Calculated values of EIS elements from the Randles circuit

Sample	R_s/ohm	R_c/ohm	Z_d	C_{dl}/mF
1-Pyramidal nanorods	5.03	0.10	9.71	2.31
2-Prismatic nanorods	5.79	0.16	10.2	2.73
3-Hexagonal nanoplates	6.31	0.45	11.71	3.01

4. Conclusions

In summary, we have demonstrated a facile approach to control the desirable morphology of h-MoO_3 nanostructures. By rationally controlling the amount of HMTA, h-MoO_3 in pyramidal nanorods, prismatic nanorods and hexagonal nanoplates-like morphologies are achieved, with an approximate molecular formula unit of $(NH_4)_{0.11}(H_2O)_{0.28}$ $MoO_{2.89}$, $(NH_4)_{0.23}(H_2O)_{0.39}$ $MoO_{2.77}$ and $(NH_4)_{0.44}(H_2O)_{0.30}$ $MoO_{2.56}$, respectively. The as-synthesized h-MoO_3 in pyramidal morphology exhibited high specific capacitance (230 F/g) compared to prismatic nanorods (160 F/g) or hexagonal nanoplates morphology (103 F/g) at an applied current density of 0.25 A/g. The coexistence of the (100) and $(\bar{1}10)$ planes in pyramidal morphology exposes various intercalation sites (HW, SW and TC) for the intercalation of electrolyte ions. The ammonium ions not only stabilize the hexagonal framework, but also facilitate the mechanism of charge-storage (by the Vehicle mechanism of proton transportation). This unique strategy to enhance the electro-kinetics leads to increase in charge-storage capacity of MoO_3. This represents the first attempt of preparing h-MoO_3 for electrochemical capacitors, delivering possibilities in catalytic, sensing and solar applications.

Acknowledgements

Vipin Kumar acknowledges the research scholarship provided by NTU and Temasek Laboratories @ NTU in Singapore.

Notes and references

[a]*School of Materials Science and Engineering, 50 Nanyang Avenue, Nanyang Technological University, Singapore – 639798 *Corresponding Email: pslee@ntu.edu.sg*

Electronic Supporting Information (ESI) available: Transmission electron microscopy (TEM) and High resolution transmission electron microscopy (HRTEM) of pyramidal nanorods; comparison of reaction times to prepared h-MoO_3 nanostructures, FTIR spectrum of pyramidal nanorods, prismatic nanorods and hexagonal nanoplates; atomic representation of hexagonal framework; Cyclic voltammograms (CVs) of pyramidal nanorods, prismatic nanorods and hexagonal nanoplates at higher scan rates; BET isotherms of all three samples; Charge/discharge profiles of pyramidal nanorods; prismatic nanorods and hexagonal nanoplates at the various current densities; FESEM images of pyramidal nanorods before and after cycling; Bode plot of pyramidal nanorods, prismatic nanorods and hexagonal nanoplates; Electrochemical performance comparison table.

1. S. Li and D. A. Dixon, *J. Phys. Chem. A*, 2006, **110**, 6231–44.
2. F. Zhou, M. Cococcioni, C. Marianetti, D. Morgan, and G. Ceder, *Phys Rev. B*, 2004, **70**, 235121.
3. P. S. Directorate and F. Monmouth, *J. Electrochem. Soc.,* 1995, **142**, 6–8.
4. H. Y. Lee and J. B. Goodenough, *J. Solid State Chem.,* 1999, **144**, 220–223.
5. B. E. Conway, *Electrochemical Supercapacitors: Scientific Fundamentals and Technological Applications*. Kluwer Academic/Plenum, New York, 1999.
6. A. C. Arias, J. D. MacKenzie, I. McCulloch, J. Rivnay, and A. Salleo, *Chem.Rev.,* 2010, **110**, 3–24.
7. M. S. Gordon, D. Dabdub, and R. B. Gerber, *Proc. Natl. Acad. Sci.,* 2009, **106**, 16889–16889.
8. X. Wang, B. D. Myers, J. Yan, G. Shekhawat, V. Dravid, and P. S. Lee, *Nanoscale*, 2013, **5**, 4119–22.
9. E. Khoo, J. Wang, J. Ma, and P. S. Lee, *J. Mater. Chem.,* 2010, **20**, 8368.
10. J. P. Zheng, P. J. Cygan, and T. R. Jow, *J. Electrochem. Soc*. 1995, **142**, 2699.
11. J. P. Zheng and T. R. Jow, *J. Electrochem. Soc*. 1995, **142**, L6.
12. H. Farsi, F. Gobal, H. Raissi, and S. Moghiminia, *J. Solid State Electrochem.* 2009, **14**, 643–650.
13. T. Brezesinski, J. Wang, S. H. Tolbert, and B. Dunn, *Nat. Mater.,* 2010, **9**, 146–51.
14. J. W. Kim, V. Augustyn, and B. Dunn, *Adv. Energy Mater.*, 2012, **2**, 141–148.
15. O. Ghodbane, J. L. Pascal and F. Favier, *ACS Appl. Mater. Interfaces*, 2009, **1**, 1130 - 1139.
16. R. L. Smith and G. S. Rohrer, *J. Solid State Chem.,* 1996, **115**, 104–115.
17. E. M. McCarron III, *J. Chem. Soc. Chem. Commun.,* 1986, **101**, 336–338.
18. J. C. Calabrese and E. M. McCarron, *J. Solid State Chem.,* 1991, **125**, 121–125.
19. V. Kumar, A. Sumboja, J. Wang, V. Bhavanasi, V. C. Nguyen, and P. S. Lee, *Chem. Mater*., 2014, **26**, 5533-5539.
20. T. Tao, Q. Chen, H. Hu, and Y. Chen, *Mater. Lett.,* 2012, **66**, 102–105.

21. G. R. Li, Z. L. Wang, F. L. Zheng, Y. N. Ou, and Y. X. Tong, *J. Mater. Chem.,* 2011, **21**, 4217.
22. V. Kumar and P. S. Lee, *J. Phys. Chem. C*, 2015, **119**, 9041-9049.
23. I. Shakir, M. Shahid, S. Cherevko, C.-H. Chung, and D. J. Kang, *Electrochimica Acta*, 2011, **58**, 76–80.
24. I. Shakir, M. Shahid, M. Nadeem, and D. J. Kang, *Electrochim. Acta,* 2012, **72**, 134–137.
25. M. S. Islam, D. J. Driscoll, C. A. J. Fisher, P. R. Slater, M. C. Group, C. Di V, V. Uni, G. Gu, and U. Kingdom, *Chem. Mater.,* 2005, 5085–5092.
26. C. Nan, J. Lu, C. Chen, Q. Peng, and Y. Li, *J. Mater. Chem.,* 2011, **21**, 9994.
27. G.-Z. Wei, X. Lu, F.-S. Ke, L. Huang, J.-T. Li, Z.-X. Wang, Z.-Y. Zhou, and S.-G. Sun, *Adv. Mater.,* 2010, **22**, 4364–7.
28. J. Jiang, J. Liu, S. Peng, D. Qian, D. Luo, Q. Wang, Z. Tian, and Y. Liu, *J. Mater. Chem. A*, 2013, **1**, 2588.
29. W. Tang, L. Liu, S. Tian, L. Li, Y. Yue, Y. Wu, and K. Zhu, *Chem. Commun.,* 2011, **47**, 10058–60.
30. J. Chang, M. Jin, F. Yao, T. H. Kim, V. T. Le, H. Yue, F. Gunes, B. Li, A. Ghosh, S. Xie, and Y. H. Lee, *Adv. Funct.Mater.,* 2013, **23**, 5074–5083.
31. L. V. Gurvisch, I. V. Veyts, C. B. Alocock, *Thermodynamic Properties of Individual Substances*, 4th edn., 1994, CRC Press, Boca Raton.
32. V. Kumar, X. Wang, and P. S. Lee, *CrystEngComm*, 2013, **15**, 7663.
33. H. J. Lunk, H. Hartl, M. A. Hartl, M. J. G. Fait, I. G. Shenderovich, M. Feist, T. A. Frisk, L. L. Daemen, D. Mauder, R. Eckelt, and A. A. Gurinov, *Inorg. Chem.,* 2010, **49**, 9400–8.
34. B. Rachid, *Ann. Chim.,* 2007, **32**, 277 - 282
35. K. M. McPeak, T. P. Le, N. G. Britton, Z. S. Nickolov, Y. A. Elabd, and J. B. Baxter, *Langmuir,* 2011, **27**, 3672–7.
36. F. Taube, M. Hashimoto, I. Andersson, and L. Pettersson, *J. Chem. Soci. Dalton Trans.,* 2002, 1002–1008.
37. V. Nardello, J. Marko, G. Vermeerch, J. M. Aubry, *Irog. Chem.,* 1995, **34,** 4950–4957.
38. M. Cindric, Z. Veksli and B. Kamenar, *Croat. Chem. Acta*, 2009, **82**, 345-367.
39. I. M. Szilagyi, J. Madrasaz, G. Pokol, P. Kiraly, G. Tarkanyi, S. Saukko, J. Mizsei, A. L. Toth, A. Szabo, K. V. Josepovits, *Chem. Mater.,* 2008, **20**, 4116–4125.
40. Y. L. Leung, P. C. Wong, K. A. R. Mitchell, and K. J. Smith, *Appl. Surf. Sci*. 1998, **136**, 4–6.
41. R. Bacsa, J. Kiwi, T. Ohno, P. Albers, and V. Nadtochenko, *J. Phys. Chem. B,* 2005, **109**, 5994–6003.
42. P. Serp and J. L. Figueiredo, *Carbon Materials For Catalysis*, John Wiley & Sons, Inc., Hoboken, New Jersey, USA, 2009.
43. H. Jiang, T. Zhao, C. Li, and J. Ma, *J. Mater. Chem.,* 2011, **21**, 3818.
44. J. S. Chen, M. F. Ng, H. Bin Wu, L. Zhang, and X. W. (David) Lou, *CrystEngComm*, 2012, **14**, 5133.
45. D. Cai, D. Wang, B. Liu, Y. Wang, Y. Liu, L. Wang, H. Li, H. Huang, Q. Li, and T. Wang, *ACS Appl. Mater. Interfaces*, 2013, **5**, 12905–10.
46. X. Wang, W. S. Liu, X. Lu, and P. S. Lee, *J. Mater. Chem.,* 2012, **22**, 23114.
47. J. Wang, J. Polleux, J. Lim, and B. Dunn, *J. Phys. Chem. C,* 2007, **2**, 14925–14931.
48. S. M. Majhi, P. Rai, S. Raj, B. Chon, K. Park, and Y. Yu, *ACS Appl. Mater. Interfaces*, 2014, **6**, 7491 - 7497.
49. K. D. Kreuer, A. Rabenau and W. Weppner, *Angew. Chem. Int. Ed. Engl.* 1982, **21**, 3.
50. K. D. Kreuer, A. Rabenau, and R. Messer, Appl. Phys. 1983, **A 32**, 45-53.
51. R. Thakkar and U. Chudasama, *J. Sci. Indus. Res*. 2009, **68**, 312–318.
52. H. Lin, F. Zhou, C. P. Liu and V. Ozolins, *J. Mater. Chem. A*, 2014, **2**, 12280-12288.
53. S. S. Mahajan, S. H. Mujawar, P. S. Shinde, A. I. Inamdar, and P. S. Patil, *Int. J. Electrchem. Sci.,* 2008, **3**, 953–960.
54. X. Wang, A. Sumboja, M. Lin, J. Yan, and P. S. Lee, *Nanoscale*, 2012, **4**, 7266–72.
55. J. Chmiola, G. Yushin, R. Dash and Y. Gogotsi, *J. Power Sources*, 2006, **158**, 765.
56. Q. Mahmood, W. S. Kim, and H. S. Park, *Nanoscale*, 2012, **4**, 7855–60.
57. I. Shakir, M. Shahid, H. W. Yang, and D. J. Kang, *Electrochim. Acta*, 2010, **56**, 376–380.
58. R. Liang, H. Cao, and D. Qian, *Chem. Commun.*, 2011, **47**, 10305–7.
59. M. Hibino, W. Han, and T. Kudo, 2000, *Solid State Ionics*, **135**, 61–69.
60. S. Balaji, Y. Djaoued, R. Z. Ferguson, and R. Bru, *Chem. Mater.,* 2009, **21**, 1381–1389.